

Towards the design of gravitational-wave detectors for probing neutron-star physics

Haixing Miao,¹ Huan Yang,^{2,3,*} and Denis Martynov^{4,1}

¹*School of Physics and Astronomy, and Institute of Gravitational Wave Astronomy, University of Birmingham, Edgbaston, Birmingham B15 2TT, United Kingdom*

²*Perimeter Institute for Theoretical Physics, Waterloo, ON N2L2Y5, Canada*

³*University of Guelph, Guelph, ON N2L3G1, Canada*

⁴*LIGO, Massachusetts Institute of Technology, Cambridge, MA 02139, USA*

The merger of binary neutron star encodes rich physics of extreme states of matter. Probing it through gravitational-wave observations requires the detectors to have high sensitivity above 1 kHz. Fortunately for current advanced detectors, there is a sizeable gap between the quantum-limited sensitivity and the classical noise at high frequencies. Here we propose a detector design that explores such a gap by pushing down the high-frequency quantum noise with an active optomechanical filter, frequency-dependent squeezing, and high optical power. The resulting noise level from 1 kHz to 4 kHz approaches the current facility limit, and is a factor of 20 to 30 below the design of existing advanced detectors at these frequencies. It will allow for precision measurements of (i) the post-merger signal of binary neutron star, with electromagnetic counterparts such as short gamma-ray burst and kilonovae, (ii) late-time inspiral, merger, and ringdown of low-mass black hole-neutron star systems, and (iii) high frequency modes during supernovae explosions and/or magnetar giant flares. This design tries to maximise the science return of current facilities by achieving a sensitive frequency band that is complementary to proposed longer-baseline third-generation detectors: 10 km Einstein Telescope, and 40 km Cosmic Explorer. We have highlighted the main technical challenges towards realising the design, which requires dedicated research programs. If demonstrated in current facilities, the technique can be transferred to new facilities with longer baseline.

I. INTRODUCTION

The discovery of a binary neutron star merger event in August, 2017 has marked the birth of multi-messenger astronomy including gravitational waves (GW) [1]. In the near future, we also expect detections of black hole-neutron star mergers. These coalescence events, with matter involved, produce copious electromagnetic (EM) radiation, e.g., short-gamma-ray burst and kilonovae [2–4], in addition to GW emission. The joint observation of both GW and EM signals in GW170817 has already led to fundamental breakthroughs in understanding neutron star equation-of-state, the origin of short-gamma-ray bursts and heavy elements in our universe [5–7].

Current advanced GW detectors mainly sense low-frequency, inspiral part of the binary neutron star (BNS), unless the source distance is within of the order of 10 Mpc. The merger phase however contains rich physics of nuclear matters under extreme conditions. In order to probe these new physics through GW observations, we need better detector sensitivity above 1 kHz by resolving various spectra signatures, such as the main peak [8], sub-dominant mode features [9], and one-arm instability [10–12]. If a sensitivity level around $5 \times 10^{-25} \text{ Hz}^{-1/2}$ from 1 kHz to 4 kHz can be achieved, which defines our target, a precise measurement of BNS post-merger waveform will become possible, and GW signals from merging NS and low-mass black hole (BH) binaries could also be observable. This may also allow an independent determination of Hubble Constant with GW observation (similar to [13] on post-merger waveforms, with other methods discussed in [14–16]), spectroscopy measurement of high fre-

quency modes during supernovae explosions and/or magnetar giant flares, and possible detection of stochastic GW background from post-merger hypermassive NSs .

The dominant noise of advanced GW detectors at high frequencies comes from the counting statistics of photon, also known as quantum shot noise. There are three different approaches to reducing the shot noise [17]: (1) increasing the power, (2) using non-classical state of light—the squeezed state [18–20], and (3) signal recycling by making the cavity resonance to coincide with the signal frequency of interest [21–24]. The third approach however is constrained by a tradeoff between the bandwidth and peak sensitivity—high peak sensitivity implies narrow detection bandwidth. We consider the use of an active optomechanical filter cavity to surpass this constraint [25, 26], together with high optical power and frequency-dependent squeezing [27, 28] to achieve the target sensitivity.

II. DETECTOR DESIGN

The proposed detector layout consists of the power recycling, signal recycling, and arm optical cavities, and is similar to the setup of Advanced LIGO [32], Advanced VIRGO [33] and KAGRA [34]. We consider two cases for the main interferometer: the first one, as an intermediate step, assumes 1064 nm light and LIGO-LF classical noise level [35]; the second one, which achieves the target sensitivity, employs 2000 nm light and has the classical noise budget of LIGO Voyager [29]. Envisioning progress in the capability of handling high-power interferometers, we assume the arm cavity power for both case are doubled with respect to their original study, i.e., having 1.5 MW and 6.0 MW, respectively. Due to the wavelength difference, the radiation pressure effect of 6 MW

* hyang@perimeterinstitute.ca

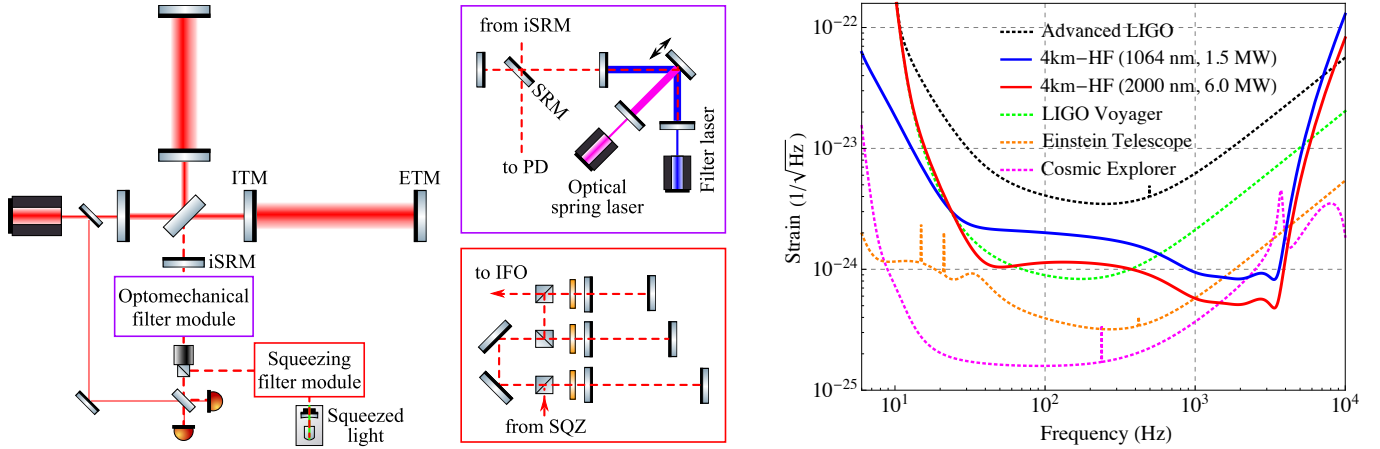


FIG. 1. Schematics showing the detector design (left) and the resulting sensitivity (right). The blue curve shows a possible intermediate step towards the target sensitivity in red. The target is around a factor of 30 below Advanced LIGO design at 3 kHz: a factor of 3 from 10dB squeezing, 2 from high power, and 5 from detuned signal recycling with the optomechanical filter extending the improvement around the detune frequency. Sensitivities of LIGO Voyager [29], Einstein Telescope [30], and Cosmic Explorer [31] are shown as references.

	Parameters	Values
Interferometer	arm length	4 km
	arm cavity power	6.0 MW (1.5MW)
	test mass	200 kg
	laser wavelength	2000 nm (1064 nm)
	temperature	120 K (295 K)
	SRM transmission	3750 ppm
	SR detune	1.5 kHz
	internal loss: ETM to SRM	≤ 800 ppm (2000 ppm)
	output loss	$\leq 3\%$ (5%)
Optomechanical filter	oscillator mirror mass	5 mg
	mirror radius, thickness	1.4 mm, 0.35 mm
	loss angle of substrate, coating	1.0×10^{-9} , 2.0×10^{-6}
	suspension quality factor	3.0×10^6
	bare frequency, optical spring	10 Hz, 12 kHz
	cavity length	4.3 m
	cavity bandwidth	1.4 kHz
	beam radius	0.52 mm
	resonating power	338 W (180 W)
	round-trip loss	≤ 5 ppm (10 ppm)
Optical spring	laser wavelength	1064 nm
	photodiode quantum efficiency	≥ 0.999
	cavity length	10 cm
	cavity bandwidth, detune	60 kHz, 0.9 MHz
	resonating power	680 W
	round-trip loss	≤ 1 ppm
SQZ filter	temperature	16 K
	squeezing (observed)	10 dB
	squeezing angle	0 rad
	filter cavity 1 (bandwidth, detune)	4.66 Hz, -42.6 Hz
	filter cavity 2	197 Hz, 3409 Hz
filter cavity 3	355 Hz, 1107 Hz	
filter cavity 4	510 Hz, -1920 Hz	

TABLE I. Parameters of the design. Values in the bracket are those used in producing the blue curve in Fig. 1.

at 2000 nm is equivalent to around 3.0 MW at 1064 nm.

Comparing to current advanced detectors, the key design difference comes from the configuration of the signal recycling cavity as shown in Fig. 1. We introduce an internal signal recycling mirror (iSRM) which forms an impedance matched cavity with the input test mass (ITM) mirror. The advantage is that the GW signal is not affected by the narrow bandwidth of the arm cavity. However, optical losses from the central beam splitter (BS) and also ITM substrate are resonantly enhanced, which puts a hard bound on the ultimate detector sensitivity [36]. The total round-trip loss between the SRM and the end test mass (ETM) mirror should be the order of 1000 ppm to reach a sensitivity around $5 \times 10^{-25} / \sqrt{\text{Hz}}$ with MW arm cavity power. This goal requires diffraction loss per optical surface to be less than 25 ppm for 1064 nm and 7 ppm for 2000 nm wavelength. Also, reflectivity of the BS and ITM anti-reflective coatings should be less than 10 ppm. Taking Advanced LIGO as an example and with these parameters which are achievable using existing technology, we set ITM transmission to 0.05 to limit the total loss, which however increases the optical load on BS by a factor of 3 compared to the Advanced LIGO design. This number can be reduced in the future, once optical surfaces with higher quality are available.

In addition to iSRM, the optomechanical filter module is added to the signal recycling cavity. This module compensates for the phase lag acquired by signal sidebands in the free space interferometer, which results in a broadband resonance of the signal [25]. The key component of the system is a high quality mechanical oscillator embedded in an optical cavity, which is pumped by an external filter laser with proper frequency and amplitude. We propose to implement the mechanical oscillator by comprising a low loss quasi-monolithic suspension [37] and a milligram-scale mirror. In order for the phase compensation work properly in kHz regime, we increase the oscillator frequency to 12 kHz by creating an optical spring with an auxiliary laser and optical cavity, which

is also called the optical dilution [38]. A higher oscillator frequency of 50 kHz would give rise to a better sensitivity; however, we do not find a technically feasible realisation, which uses the optical spring effect and at the same time meets the noise requirement.

Fluctuation of the oscillator around its resonant frequency should be kept below a certain value, since it is directly down converted to the GW band. There are five major noise sources: suspension thermal noise, quantum radiation pressure noise from the optical spring, coating thermal noise, substrate Brownian noise, and thermoelastic noise. The key challenges to suppress these noises go as follows. First of all, total optical loss of the optical spring cavity should be kept below 1% in order to cancel the radiation pressure noise in the optical spring using the scheme in Ref. [39]. This requires photodiodes with high quantum efficiency [40], adaptive mode matching [41], and high-quality cavity mirrors to achieve round trip loss of 1 ppm inside a cm long high-finesse cavity. The required level of mechanical dissipation in optical coatings and milligram-size mirror substrate could be achieved by using a low-loss silicon mirror with crystalline coatings [42] cooled down to 16 K (coefficient of expansion zero-crossing temperature) [43]. We assume a coating loss angle to be a factor of a few below the state of the art as a projection to the near future, given the progress of the field. Finally, the resonant frequency of the oscillator should be significantly lower than body modes of the mirror, which is the case for this 12 kHz realisation.

Finally, the squeezing filter module consists of a cascade of optical cavities, which is to create frequency-dependent squeezing for reducing the quantum noise over a broad frequency band [20, 27, 28]. This design requires four filter cavities to reach the optimal frequency-dependent squeezing angle. In the conventional detuned signal recycling configuration, two filter cavities are needed [44]—one for reducing the low-frequency radiation-pressure noise, and one for undoing the squeezing angle rotation from the detuned interferometer. Two extra filter cavities are required here because of additional frequency dependence introduced by the optomechanical filter. Among these four filter cavities, the first one for reducing the radiation pressure noise has the lowest cavity bandwidth, which implies a long cavity length due to limitations from the optical loss. If we focus on only the sensitivity above 100 Hz, it can be removed. Alternatively, we can apply the recently proposed idea of using the arm cavities as the squeezing filter [45]. Three additional filter cavities with length around ten meters are essential for reaching the target sensitivity at high frequencies.

The resulting sensitivity curves are shown in Fig. 1, and the key parameters are summarised in Table I. The detailed noise budget and other information are provided in the Supplementary Material. In the following discussion, we will present the science case of this this high-frequency detector design with its target sensitivity.

III. SCIENTIFIC RETURN

In the section, we discuss several key scientific returns of this high-frequency detector design with its target sensitivity, including spectroscopy of BNS post-merger waveform, observation of low mass BH-NS merger/post-merger dynamics, detection of high-frequency stochastic GW background, and measurement of Hubble Constant in the absence of EM counterparts. These scenarios are all related to physical processes difficult to probe with low-frequency GW observations. In addition to those focused here, more scientific goals are open for exploration in the high-frequency band from 1 kHz to 4 kHz, e.g., for detecting high-frequency modes during core-collapse supernovae explosions and magnetar giant flares (see the Supplementary Material for discussions).

A. Precise spectroscopy of BNS post-merger dynamics

Comparing to their progenitors before merger, these NS merger remnants contain extremely hot, dense nuclear material in non-equilibrium state. Magneto-rotational instabilities and magnetic winding likely boost the magnetic field to the order of 10^{15} G level, and the quenching superconducting cores produce abundant neutrinos. A precise GW spectroscopy measurement for NS Helioseismology, and the joint observation of post-merger GW and electromagnetic waves (e.g., gamma-ray burst and kilonovae) shall help us to explore these most violent, matter-involving processes in the universe.

There are many progresses towards understanding post-merger dynamics and GW signature of the merger remnant. The signal spectrum could contain several characteristic peaks, which are postulated to be related to modal evolution of the merger remnants. These spectra signatures are time dependent, and also sensitive to the star equation of state, individual masses, initial rotations, and possibly magneto-hydrodynamic instabilities, which have not been fully implemented in current simulations. Therefore we focus on the dominant peak contribution as an example, which is one of the main spectra features and now understood in a more robust manner. This analysis can be extended by incorporating the entire post-merger waveform assuming that it can be accurately modelled (see e.g., Ref. [9, 46]).

As shown in Fig. 2, we apply Monte-Carlo (MC) method to generate Mock data for binary neutron star merger events. For binary neutron systems in each MC realization, we randomly sample the sky location, inclination angles, component masses (according to the distribution in [47]), and distances to earth (by assuming uniform merger rate $1540\text{Gpc}^{-3}\text{yr}^{-1}$ in co-moving volume [1]) in one year timescale, and only keep the events with highest modal SNR and those passing detection threshold $\text{SNR} = 5$. We have computed 10^2 MC realizations in total. In Fig. 2, we present the averaged number of detections versus the expected top SNR (median value out of top events in all MC realizations) in one year for various EOS covering a wide range of possibilities. We can see that the dominant peak oscillation is expected to be captured by this high-frequency detector in one-year timescale. Following

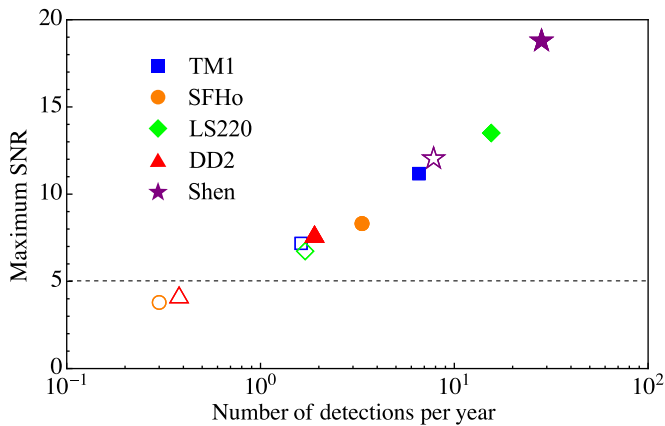


FIG. 2. Expected SNR of the 22 mode of the loudest event versus expected number of event (within one-year observation) with 22 mode detection. Each EOS has two points, with the filled one associated with high frequency detector and the unfilled one assuming the sensitivity of Cosmic Explorer to illustrate the complementary aspect of this design with respect to longer-baseline third-generation detectors.

the methodologies in [8, 9, 46], it shall be straightforward to analyze the power of this high frequency detector in distinguishing different EOS and measuring the star radius.

In addition, as shown in the Supplementary Material, precise measurements of the post-merger modes could give us redshift information of the source, because the redshift scalings of inspiral and post-merger BNS waveforms are generally different. For example, the frequency of inspiral waveform decreases with increasing total mass, and the frequency of post-merger waveform increases with increasing total mass (at least for the peak mode). Combining with the distance measurement from the GW amplitude and assuming accurate understanding of NS EOS (based on a few loud events with EM counterparts for calibration), this may allow a determination of Hubble Constant to an accuracy of the order of $0.1/\sqrt{N}$ (N is the number of stacked events) even in the absence of EM counterparts.

B. Neutron star-black hole binary

The discovery of GW150914 and the following observations on binary black hole mergers have drawn much attention onto heavy stellar-mass black holes as they emit stronger GWs, and that part of their progenitor stars may form in low-metallicity environment. Low mass BHs (LMBHs), on the

TABLE II. SNRs for different types of BH-NS mergers

Type	$M_{\text{NS}} (M_{\odot})$	$M_{\text{BH}}/M_{\text{NS}}$	SNR_{CE}	SNR_{HF}	$f_{\text{cut}}(\text{kHz})$	$d (\text{Mpc})$
I	1.35	1.5	2.58	3.17	1.8	50
I	1.35	2	1.31	1.67	1.9	50
II	1.35	3	3.65	6.59	2.4	50
III	1.35	4	3.07	5.25	2.4	50
III	1.35	5	4.2	6.33	2.2	50

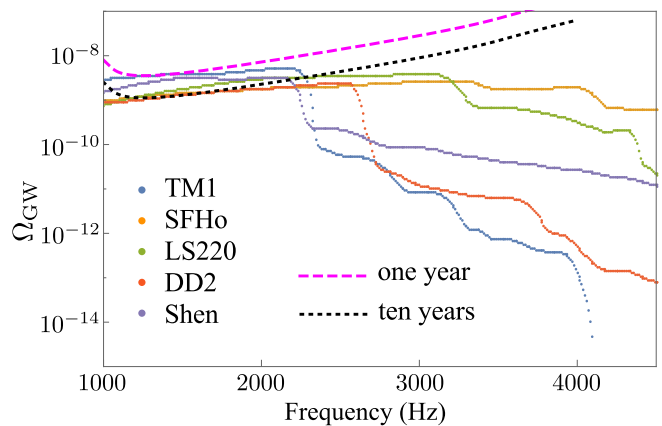


FIG. 3. Stochastic GW background produced by post-merger GW emission of BNS systems. The transition regions between different plateaus correspond to loudest modes in the post-merger waveform, with the main transitions associated with the 22 mode. The Magenta (Black) Dashed lines are the “power-law integrated” sensitivity curves defined in [50], corresponding to one/ten year(s) integration time respectively.

other hand, are also interesting as they could come from completely different progenitors [48]. Gravitational wave observations will be able to produce an independent measure of the properties of such systems, including mass, spin distributions, and the cosmological evolution. In particular, the coalescence of a neutron star and a LMBH may emit gravitational waves above 1 kHz, which can be also jointly detected with electromagnetic waves generated from tidal disruption of the NS, mass accretion into the BH, etc, as another fruitful scenario for multi-messenger astronomy.

Based on the classification and simulations performed in Ref. [49], We compute the SNR of merger/post-merger waveform for BH/NS systems (Table II), assuming $\Gamma = 2$ polytropic EOS, binary distance distance at 50Mpc and CE/high-frequency detector sensitivity. The cut-off frequency f_{cut} denotes the starting frequency of merger/post-merger waveform ([49]). Type I, II, III waveforms may be intuitively understood as tidal disruption outside ISCO (Innermost-Stable-Circular-Orbit), inside ISCO and no disruption respectively.

C. Stochastic gravitational wave background

At frequencies above 1kHz, the component of stochastic GW background (SGWB) contributed by binary BHs is significantly reduced [1], and the SGWB is likely dominated by wave emissions from BNSs. As the inspiral part of BNS waveform cuts off sharply before the BNS ISCO and/or contact frequency which are typically below 1.4kHz, here we present a study on the contribution to SGWB by BNS post-merger hydrodynamical oscillations (Fig. 3) [51]. Such component displays interesting plateau signatures associated with the main post-merger modes, which has not been discussed in previous literature, and becomes the dominant source of SGWB above the ISCO frequency (also see [52, 53] to com-

pare with estimates for magnetar emissions). We find that ten-year observation of the high frequency detector may be able to resolve (SNR above 3 [1]) SGWB for some of the EOS considered here. We also would like to emphasize that this high-frequency window provides new opportunities to search for SGWB of primordial/exotic origins, because of low astrophysical confusion noise.

IV. DISCUSSION

This study illustrates both challenges in improving the high-frequency sensitivity of GW detectors and the exciting neutron-star science that is accessible by exploring this new frequency band. For the detector design, we have not exhausted all the possibilities for achieving the target sensitivity. The essential elements, e.g., squeezing, low optical loss, and high power, will however be common to different designs. Additionally, the optomechanical filter is not the only approach for broadening detection bandwidth, and there are others based upon atomic systems [54–56]. Pushing the limit of these elements and different approaches define the direction of future research towards building high-frequency detectors. Once the techniques are well tested in current facilities, implementing them to facilities with longer arm lengths will allow even better sensitivity and richer science returns. For example, a factor of 5 improvement may enable GW spectroscopy measurement of isolated NSs during the giant flare phase of magnetars [57]. High frequency part (> 1 kHz) of post-bounce GWs of supernovae might be detected up to several Mpcs. Post-mergers of BNS systems can be observed to much larger distances, which allows much further GW Hubble Constant measurement and/or constraints on expansion history of the universe. We will be able to probe astrophysical processes and test predictions of General Relativity at cosmological distances, complementary to information obtained from the low-frequency GW observations.

V. ACKNOWLEDGEMENTS

We would like to thank Chunnong Zhao, Alberto Vecchio, Luis Lehner, Yiqiu Ma, Andreas Freise, Conor Mow-Lowry, Rainer Weiss, Peter Fritschel, Matthew Evans, and members of the LSC AIC, MQM, and QN groups for fruitful discussions. H.M. is supported by UK STFC Ernest Rutherford Fellowship (Grant No. ST/M005844/11). H.Y. was supported in part by Perimeter Institute for Theoretical Physics. Research at Perimeter Institute is supported by the Government of Canada through Industry Canada and by the Province of Ontario through the Ministry of Research and Innovation. D.M. acknowledge the support of the NSF and the Kavli Foundation.

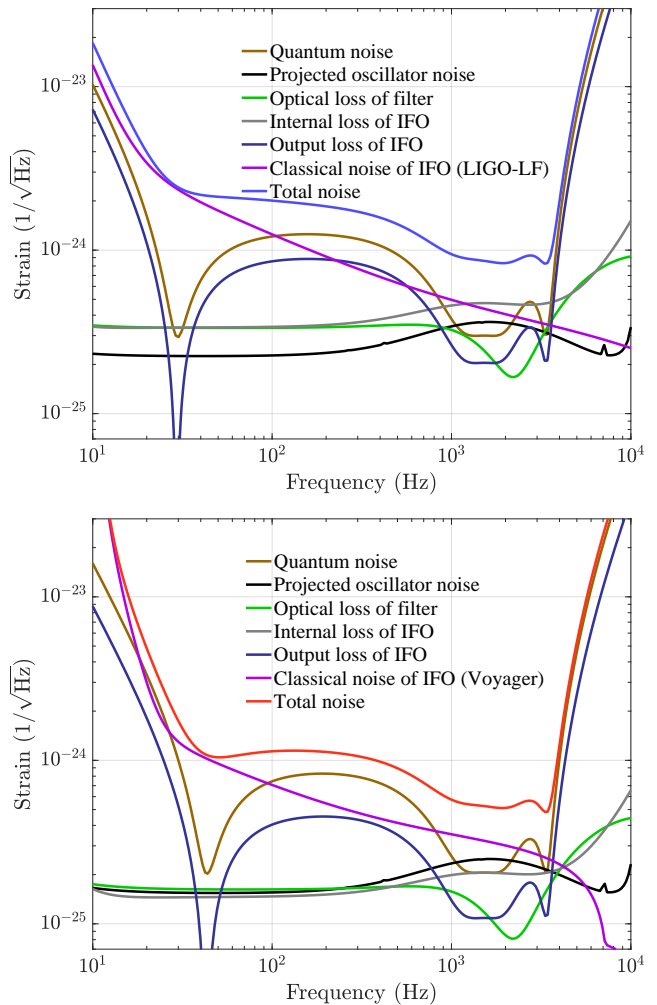


FIG. 4. The noise budget for the two cases of main interferometer: one assuming 1064 nm and LIGO-LF classical noise (upper), and the other assuming 2000 nm and LIGO Voyager classical noise (lower). The final sensitivity curves (total noise) were shown in Fig. 1 of the main text. The projected oscillator noise is coming from the mechanical oscillator in the optomechanical filter. The effect of the optical loss at different places are also included.

Appendix A: Supplemental Material

1. Noise budget

The noise budget of our design is shown in Fig. 4. The classical noise from the main interferometer is based upon previous design studies for LIGO-LF and LIGO Voyager. In addition, we have included noises from the mechanical oscillator in the optomechanical filter, and contributions from optical loss of the main components. The details are provided in the following two subsections.

2. Realisation of the optomechanical filter and its noise

In this section, we discuss the experimental realisation of the optomechanical filter and noises associated with the mechanical oscillator.

We propose to implement the oscillator using a $m = 5$ mg mirror suspended with fused silica fibers. The eigen frequency is around 10 Hz with typical quality factor of 10^6 to 10^7 . In order for the optomechanical filter to compensate the propagation phase of signal sidebands properly, as shown in Ref. [25], we need to be in the parameter regimes: $\omega_m \gg \gamma_f > \Omega$, where ω_m is the eigen frequency of the oscillator, γ_f is the filter cavity bandwidth, and Ω is the frequency of GW. To meet this requirement, we shift the eigen frequency of the oscillator up by using the optical spring effect (optical dilution [38]): $\omega_m = \sqrt{\omega_{m0}^2 + \omega_{OS}^2} \approx \omega_{OS}$ with ω_{m0} being the bare frequency. The optical spring frequency is given by the equation:

$$\omega_{OS}^2 = \frac{32\pi P_{OS}}{\lambda T_{OS} c m} \frac{\kappa}{1 + \kappa^2}, \quad (\text{A1})$$

where T_{OS} is transmission of the input coupler, P_{OS} is optical power resonating in the cavity, and $\kappa = \Delta_{OS}/\gamma_{OS}$ is the ratio between the cavity detune and bandwidth. For the optimal performance of the optomechanical filter, we need to achieve $\omega_{OS}/(2\pi) \geq 50$ kHz for having phase compensation up to several kHz. However, this requires significant optical power resonating in the cavities and strict requirements for the optical losses. These requirements can not be met using current technology but might possibly be achieved in the future. For the current realization, we have $\omega_{OS}/(2\pi) = 12$ kHz. Such an optical spring frequency degrades the quantum-limited sensitivity of the GW detector in the frequency range 3 – 4 kHz compared with the ideal scenario. But the ultimate sensitivity is still significantly lower than the current detectors.

The optical spring also allows us to dilute suspension thermal noise around ω_{OS} . This is particularly important for the ultimate filter performance since motion of the mechanical oscillator at $\omega_{OS} - \Delta_{SR} + \Omega$ (Δ_{SR} is the SR detune frequency) is directly down converted to GW band at frequency Ω . However, the optical spring also amplifies the surface motion of the oscillator from coating and substrate thermal noises, as any displacement noise will appear as a force noise when multiplying the spring constant. In addition, there is extra quantum radiation pressure noise on the oscillator exerted by the same optical field that creates the optical spring. This noise can be reduced using the suppression technique described in [39] based upon measurement feedback. There will still be residue radiation pressure noise due to optical loss inside the cavity, non-unity quantum efficiency of the photodetector, and frequency-dependent part of the noise that cannot be suppressed with feedback. The residual radiation pressure noise on the mirror is given by the equation

$$S_{FF}^{\text{rad}}(\Omega) = \frac{2\hbar m \omega_{OS}^2}{\kappa} \left[\frac{\epsilon}{T_{OS}} + (1 - \eta) + \frac{\Omega^2}{\gamma_{OS}^2} \frac{\kappa^2}{(1 + \kappa^2)^2} \right], \quad (\text{A2})$$

where ϵ is the round-trip optical loss of the cavity, η is the quantum efficiency of the photodiode that is used in the

measurement-based feedback. In addition to the indirect path from the optical spring, coating thermal noise and substrate Brownian noise of the oscillator mirror also directly enters the signal beam in terms of displacement noises. The coherence of these two paths are ignored in our analysis, which is particularly valid for the case when the laser wavelength for the optical spring cavity and the optomechanical filter are different.

If we sum up all the above mentioned noises and view them as from a single dissipative process with viscous damping, we can use a single figure of merit to summarise the noise requirement: T_{env}/Q_m , where T_{env} is the environmental temperature, and Q_m is the equivalent quality factor around the oscillator frequency after accounting for all the noises. Because the thermal noise of the mechanical oscillator degrades the sensitivity in a way similar to the optical loss, we can convert the figure of merit into the magnitude of an effective optical loss, according to Eq. (13) in Ref. [25]:

$$\epsilon_{\text{eff}} = \frac{4k_B}{\hbar \gamma_{\text{opt}}} \left(\frac{T_{\text{env}}}{Q_m} \right), \quad (\text{A3})$$

where γ_{opt} needs to be equal to c/L_{arm} for the phase compensation. Since the optomechanical filter is embedded in the interferometer, the above loss can be viewed as an internal loss. According to Ref. [36], the ultimate sensitivity one can achieve given the internal optical loss of magnitude ϵ is

$$S_{hh}^{\text{Loss}} = \frac{\hbar c^2 \epsilon}{4L_{\text{arm}}^2 \omega_0 P_{\text{arm}}}, \quad (\text{A4})$$

where P_{arm} is the arm cavity power and ω_0 is the laser frequency. To achieve a noise level of $S_{hh}^{1/2} = 5 \times 10^{-25} / \sqrt{\text{Hz}}$ given 6 MW power and 2000 nm, the total internal loss needs to be smaller than 10^4 ppm, or equivalently,

$$\frac{T_{\text{env}}}{Q_m} \leq 1.4 \times 10^{-9} \text{ K}. \quad (\text{A5})$$

Having above considerations, we come up with those numbers in Table I of the main text, and the resulting magnitude of different noises of the oscillator are shown in Fig. 5. We are able to satisfy the requirement at frequency range $1\text{kHz} \leq \Omega/(2\pi) \leq 4\text{kHz}$ given $\Delta_{SR}/(2\pi) = 1.5\text{kHz}$. In particular, the equivalent T_{env}/Q_m is around 1.6×10^{-10} K. However, the effect of internal loss is enhanced by a factor of 2, because the interferometer is detuned, and the quadrature that we decide to measure for optimising the low-frequency sensitivity is not the optimal one for suppressing the effect of internal loss. The total contribution from all noises in the oscillator to the final sensitivity is approximately equal to $2.5 \times 10^{-25} / \sqrt{\text{Hz}}$ around 2 kHz for 2000 nm case, as shown in Fig. 4.

3. Quantum noise analysis

In this section, we will provide the detail of how we perform the quantum noise analysis. The four relevant sideband fields are (1) $\omega_0 - \Omega$, (2) $\omega_0 + \Omega$, (3) $\omega_0 + 2\omega_m - 2\Delta_{SR} - \Omega$

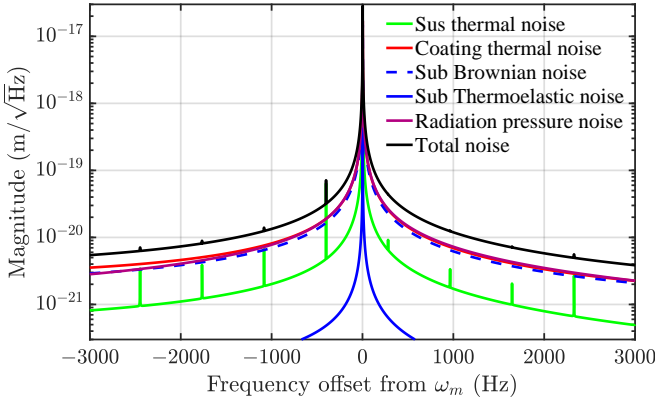


FIG. 5. Displacement noise of the mechanical oscillator near 12 kHz resonant frequency (the reference frequency) before the control laser for the optomechanical filter is tuned on, which will modify the mechanical susceptibility. Configuration of the optical spring cavity and optomechanical filter cavity was chosen to achieve total noises below the requirement in Eq. (A5).

and (4) $\omega_0 + 2\omega_m - 2\Delta_{\text{SR}} + \Omega$, as illustrated in Fig. 6. The first two sidebands are our signal sidebands, which get mixed up due to the radiation pressure coupling between light and test masses in the main interferometer; the latter two are idler sidebands, and come into the picture due to the radiation pressure coupling in the optomechanical filter cavity.

The quantum-limited sensitivity can be obtained by using the standard formalism [27, 58, 59]. It involves analysing the propagation of these sidebands (or equivalent amplitude and phase quadratures) throughout the system, and obtaining the input-output relation at the differential port of the interferometer. The key transfer matrix involved in this analysis are illustrated in Fig. 7 (a simplified schematics of the configuration in Fig. 1 of the main text): \mathbf{M}_{IFO} is the matrix for the main interferometer, \mathbf{M}_{OPT} for the optomechanical filter and \mathbf{M}_{SQZ} for the squeezing filter module and squeezed light source. Also in the same figure, \mathbf{a} is the input of above mentioned sidebands and \mathbf{b} is the output. To account for imperfections, we also include vacuum fields v_1 (from optical loss in IFO), v_2 (loss

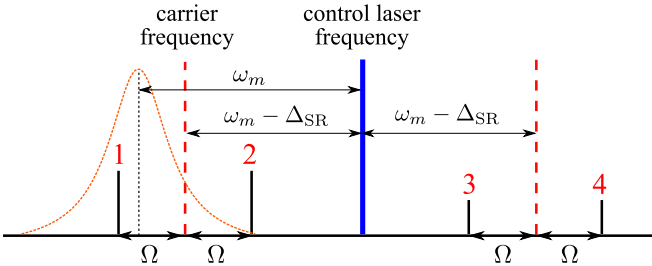


FIG. 6. A schematics shows the relevant 4 sidebands, and their frequencies with respect to the carrier frequency ω_0 and control laser frequency $\omega_0 + \omega_m - \Delta_{\text{SR}}$ (Δ_{SR} is the signal recycling detune frequency of the interferometer). The control laser is detuned away from the optomechanical cavity resonant frequency by ω_m ; the resonance profile of the cavity is illustrated by the Lorentzian shape.

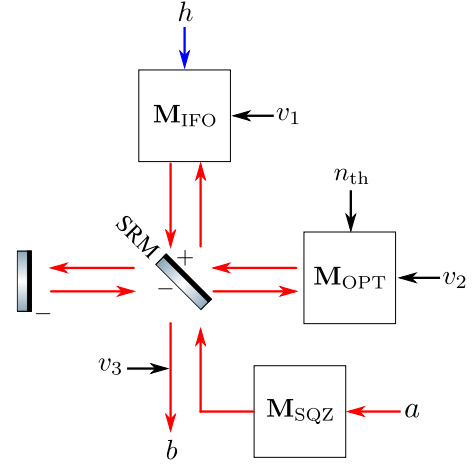


FIG. 7. The schematics shows the relevant fields, noises, GW signal, and the propagation transfer matrices involved in obtaining the input-output relation for calculating the sensitivity curve.

in optomechanical filter), v_3 (loss at the output), and thermal field n_{th} (thermal noise of the optomechanical filter). These additional fields also propagate throughout the system and finally add to the output \mathbf{b} .

Because we introduce iSRM to form an impedance matched cavity with ITM, the signal sideband part of \mathbf{M}_{IFO} is identical to that of a simple Michelson, apart from the power being the arm cavity power and the mass being replaced by the reduced mass $M/2$ ($M = 200\text{kg}$ with our specification). The idler sidebands around $\omega_0 + 2\omega_m - 2\Delta_{\text{SR}}$, when beats with carrier light at ω_0 , exert a radiation pressure on the test mass at frequency around $2\omega_m - 2\Delta_{\text{SR}}$ (tens of kHz). This is at a much higher frequency than the test-mass pendulum frequency (around 1Hz); we can therefore ignore their radiation pressure effect on the test mass and view them freely propagating through the arm cavity.

The transfer matrix \mathbf{M}_{OPT} of the optomechanical filter is the same as a detuned optomechanical cavity, which has been extensively studied in the literature (see e.g. review article [60]). However, one usually only looks at a pair of sidebands around the laser frequency (equal to $\omega_0 + \omega_m - \Delta_{\text{SR}}$ in our case). Here we need to include two pairs: 1&4, and 2&3, which are pairing between signal and idler sidebands. When the filter cavity bandwidth is much smaller than the mechanical frequency, the so-called resolved-sideband limit, the idler sidebands can be ignored, which can give rise to a rather simple input-output relation (like a negative bandwidth cavity) as shown in Ref. [25]. However, given the parameters that we have chosen, we are not in the ideal resolved-sideband limit. Interestingly, their influence on the signal sidebands can be coherently suppressed as long as they are not resonant inside the interferometer, i.e., the accumulated propagation phase for $\omega_0 + 2\omega_m - 2\Delta_{\text{SR}}$ differing from integer numbers of 2π , which is assumed in our analysis.

The transfer matrix \mathbf{M}_{SQZ} for the squeezing has two parameters: the squeezing factor and angle. We only include squeezing for the signal sidebands and leave the idler side-

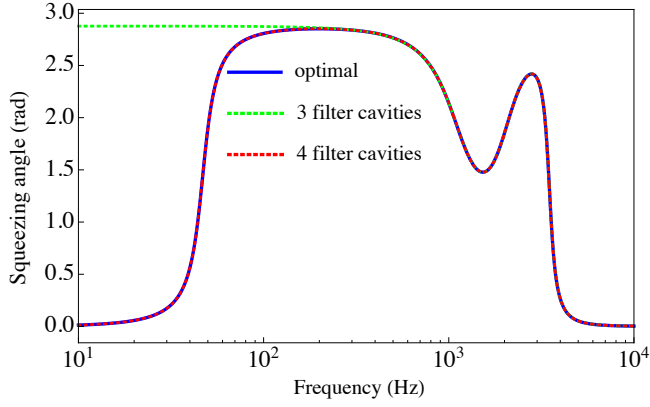


FIG. 8. The realisation of frequency-dependent squeezing angle with three or four filter cavities. The four-cavity realisation matches the optimal one at all frequencies of interests, while the three-cavity realisation matches the optimal one above 100 Hz.

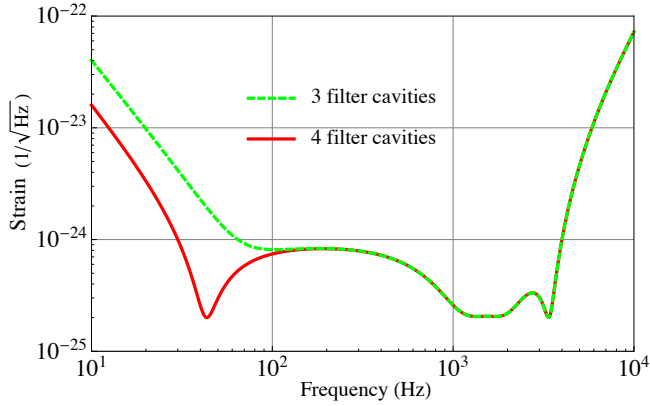


FIG. 9. The corresponding sensitivity curves (quantum noise only) for the two realisations with three and four squeezing filter cavities.

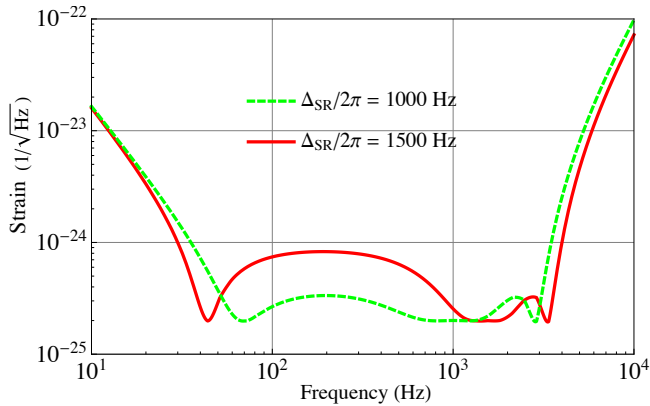


FIG. 10. Plot illustrating the effect of signal-recycling detune frequency Δ_{SR} on the quantum-limited sensitivity.

bands in the vacuum state. The squeezing factor is assumed to be 10dB observed at the final output; the squeezing angle is frequency dependent by sending the squeezed light through

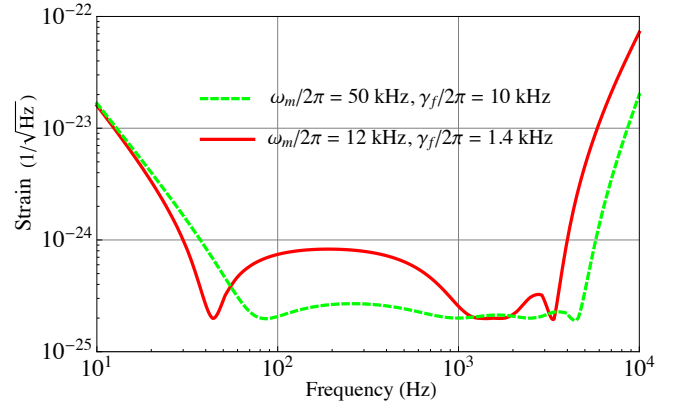


FIG. 11. Plot showing how different values of the mechanical resonant frequency ω_m influence the sensitivity.

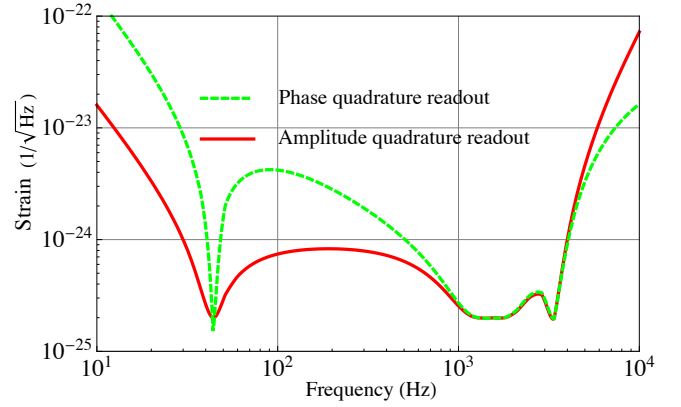


FIG. 12. Plot showing how choices of the readout quadrature affect the sensitivity.

a cascade of filter cavities. The optimal frequency-dependent squeezing angle is derived by using the approach discussed in Ref. [44]. The parameters for the filter cavities shown in Table I of the main text are obtained using the standard numerical fitting algorithm. As shown in Fig. 8, we can match the optimal frequency-dependent angle with four filter cavities. If we focus on frequencies above 100 Hz, three filter cavities will be sufficient. Fig. 9 shows the resulting sensitivity curves for these two cases.

In Fig. 10, we show how the quantum-limited sensitivity changes with respect to the signal-recycling detune frequency. Pushing the high-frequency sensitivity by increasing the detune frequency is at a price of sacrificing the sensitivity at intermediate frequencies. We choose $\Delta_{SR}/(2\pi) = 1.5$ kHz to get a good sensitivity up to 4kHz, and at the same time, have the intermediate-frequency sensitivity to be close to the classical noise budget.

In Fig. 11, we show the effect of mechanical oscillator frequency on the sensitivity. A higher oscillator frequency allows a large bandwidth γ_f for the optomechanical filter while still approximately within the resolved-sideband limit. Since γ_f sets the upper limit of detector bandwidth, we can push the sensitivity curve to a higher frequency with a high-frequency

oscillator. However, it is much more challenging to achieve 50 kHz using the optical spring effect based upon the current technology. That is why we have chosen 12 kHz as a compromise between the sensitivity and experimental feasibility. If there are other approaches to realising low-loss mechanical oscillator at low temperature in the future, we can then consider high-frequency oscillators to achieve better sensitivity.

In Fig. 12, we show how the readout quadrature affects the sensitivity. In obtaining the sensitivity in Fig. 1 of the main text, we have assumed the measurement of amplitude quadrature to get a better low-frequency sensitivity than the phase-quadrature readout. This implies that we need a balanced homodyne detection scheme, which is planned to be implemented in the near-term upgrade of advanced detectors.

4. Neutron star binaries

In the main text of the paper, we have picked five representative EOS that cover a range of stiffness with corresponding neutron star maximum mass above $2M_\odot$. These popular EOS all take into account finite temperature effect self consistently. For equal mass $1.35M_\odot + 1.35M_\odot$ neutron star binaries at distance $d = 100\text{Mpc}$, the following figure (Fig. 13) shows the post-merger waveforms for each EOS.

Based on these numerical waveforms, we identify the 22 modes and assume that they can be approximately described by decaying sinusoidal functions [8, 64]

$$h(t) = A' \frac{50\text{Mpc}}{d} \sin(2\pi f_{\text{peak}} t - \phi_0) e^{-\pi f_{\text{peak}} t / Q} \Theta(t), \quad (\text{A6})$$

where d is the distance to earth, A' is the mode amplitude, f_{peak} is the oscillation frequency, Q is the quality factor, $\Theta(t)$ is a Heaviside function and ϕ_0 is the initial phase corresponding to the choice of starting time. These parameter can be obtained by fitting the 22 peak with frequency domain expression of Eq. (A6), with more detailed procedure explained in [8]. Their

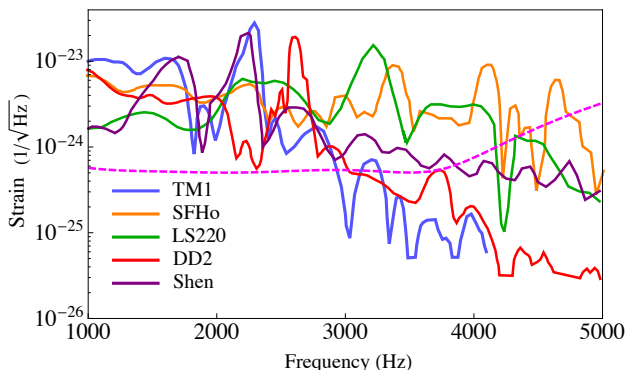


FIG. 13. Binary neutron star post-merger waveforms for different EOS extracted from [61–63], assuming a $1.35M_\odot + 1.35M_\odot$ neutron star binary located 100Mpc away from earth. The Magenta dashed line represents the sensitivity of the high frequency detector under Phase II design.

fitted values are listed in Table III with additional information on the star radius and threshold mass for prompt collapse.

EOS	$R_{1.6M_\odot}$	f_{peak} (kHz)	$\frac{M_\odot}{m_1+m_2}$	$\frac{A'(50\text{Mpc})}{10^{-22}}$	Q	$\frac{M_{\text{thres}}}{M_\odot}$
SFHo	11.77	1.21		2.7	25.7	2.95
LS220	12.5	1.09		4.3	25.7	3.05
DD2	13.26	0.98		2.8	12.7	3.35
Shen	14.42	0.84		5.0	23.3	3.45
TM1	14.36	0.85		2.5	34.2	3.1

The actual amplitude of gravitational wave measured by a gravitational-wave detector is affected by the sky location of the sources with respect to the detector, as well as the inclination of the source. Follow the convention in [65], we define the antenna pattern function of the detector as

$$F_+ = \frac{1}{2}(1 + \cos^2 \theta) \cos 2\phi \cos 2\psi - \cos \theta \sin 2\phi \sin 2\psi, \\ F_\times = \frac{1}{2}(1 + \cos^2 \theta) \cos 2\phi \sin 2\psi + \cos \theta \sin 2\phi \cos 2\psi, \quad (\text{A7})$$

Here θ, ϕ are the angular coordinates of the source in the detector's frame, and ψ is the polarization angle. The amplitude fraction in each polarization is

$$\mathcal{A}_+ = F_+ \frac{1 + \cos^2 \zeta}{2}, \quad \mathcal{A}_\times = F_\times \cos \zeta, \quad (\text{A8})$$

with ζ being the inclination angle between the line of sight and the normal direction of the orbit plane. The overall amplitude of gravitational wave measured by a given detector receives a factor of $A_r = \sqrt{\mathcal{A}_+^2 + \mathcal{A}_\times^2}$ modulation: $h(t) \rightarrow A_r h(t)$.

In performing the Monte-Carlo simulation, we have randomly sampled BNS system in sky locations, polarization angle, and inclination angle. In addition, we assume that each component mass within the binary follows the distribution [47]

$$P(m_i; M_0, \sigma) = \frac{1}{\sqrt{2\pi}\sigma} \exp\left[-\frac{(m_i - M_0)^2}{2\sigma^2}\right], \quad (\text{A9})$$

with $M_0 = 1.33M_\odot$ and $\sigma = 0.09M_\odot$. We also adopt the fitting formula for the frequency of 22 mode [66]

$$\frac{f_{\text{peak}}}{\text{kHz}} = \frac{m_1 + m_2}{M_\odot} \left[a_2 \left(\frac{R_{1.6M_\odot}}{1\text{km}} \right)^2 + a_1 \frac{R_{1.6M_\odot}}{1\text{km}} + a_0 \right]. \quad (\text{A10})$$

Here $a_0 = 5.503$, $a_1 = -0.5495$ and $a_2 = 0.0157$ are EOS-independent parameters. $R_{1.6M_\odot}$ is the radius of a non-rotating NS with gravitational mass $1.6M_\odot$, which encodes the EOS dependence.

For each EOS listed in Table. III, We have performed 100 Monte-Carlo realizations. In each realization, for one-year observation period, we randomly generate source parameters of binary neutron stars with $z \leq 0.2$ (component masses, distance, inclination angle, sky location, polarization angle) according to Eq. (A9), Eq. (A10) and the merger rate $R_m =$

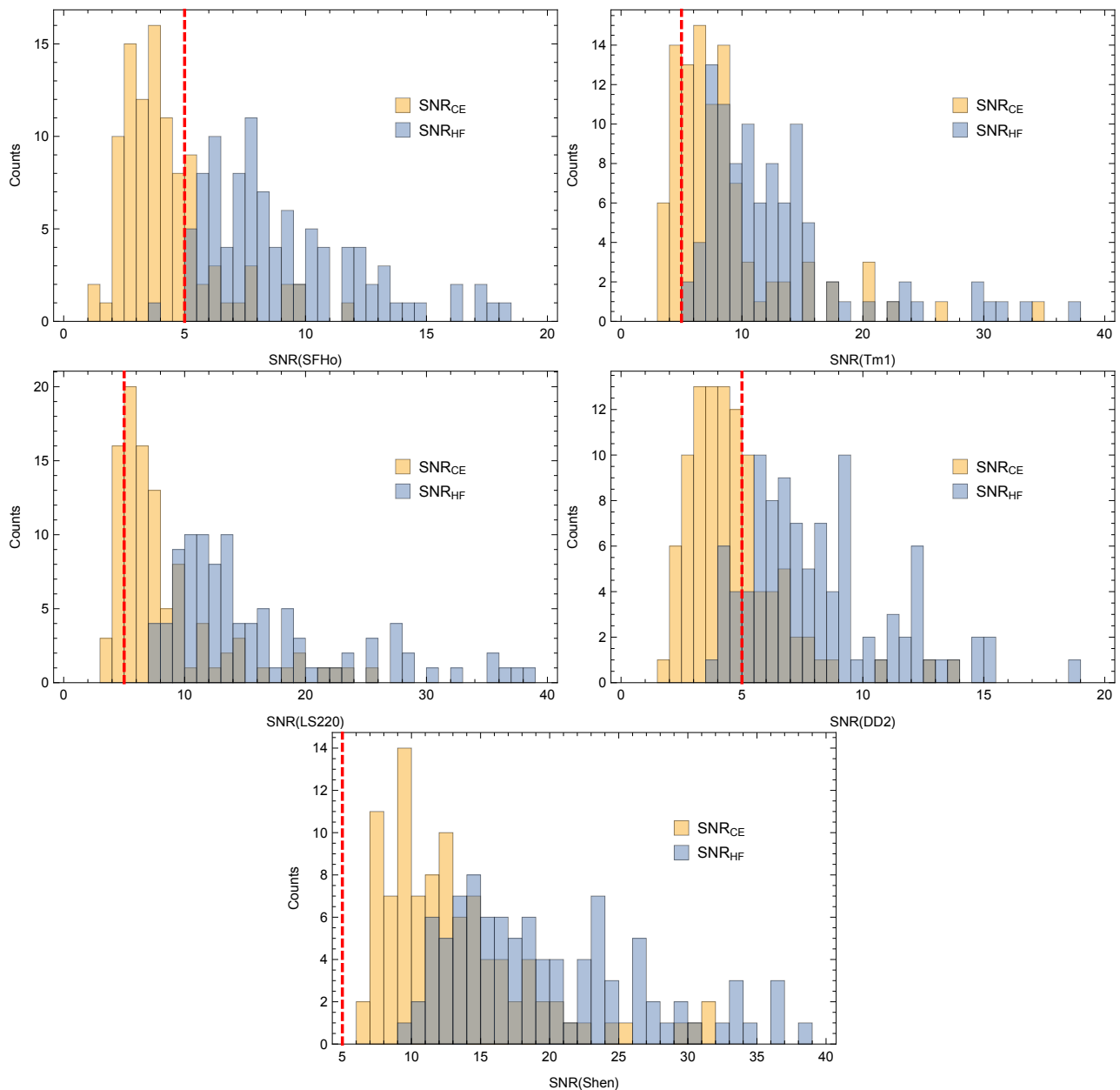


FIG. 14. Histogram for the Monte-Carlo study performed in this work. For each Monte-Carlo realization, we record the SNR of the top event and compare the performance between the high-frequency detector and Cosmic Explorer. The corresponding EOSs are “SFHo”, “TM1”, “LS220”, “DD2”, and “Shen”. For “Shen EOS”, both detectors are expected to observe a high SNR event for the 22 mode after one year observation.

$1540 \text{ Gpc}^{-3} \text{ yr}^{-1}$ which is based on the most recent estimate in [1]. We pick the top SNR event from each Monte-Carlo realization, and collect them in histograms shown in Fig. 14. For “SFHo” EOS, which is an extreme case, there is about 12% chance for Cosmic Explorer to detect a 22 mode oscillation after one-year observation, while the number for the high frequency detector is 99%. For other EOS, there are many events above detection threshold for both Cosmic Explorer and the high-frequency detector. In Fig. 2 in the main text, for each EOS, we summarize the median number of events with 22-mode detection and the median SNR for the best event in all

Monte-Carlo realizations.

5. Stochastic gravitational wave background

The stochastic gravitational wave background (GWB) is often characterised by

$$\Omega_{\text{GW}}(f) \equiv \frac{1}{\rho_c} \frac{d\rho_{\text{GW}}}{d \log f} = \frac{8\pi G}{3c^2 H_0^2} \frac{d\rho_{\text{GW}}}{d \log f}, \quad (\text{A11})$$

with ρ_c being the critical energy density of the universe and $H_0 \approx 67.8 \text{ km/sMpc}^{-1}$ is the Hubble's constant. The GWB generated by certain type of source θ_k can be computed by

$$\Omega_{\text{GW}}(f; \theta_k) = \frac{f}{\rho_c H_0} \int_0^{z_m} dz \frac{R(z; \theta_k) \frac{dE_{\text{GW}}}{df}(f_s; \theta_k)}{(1+z) \sqrt{\Omega_M(1+z)^3 + \Omega_\Lambda}}, \quad (\text{A12})$$

where $f_s = f(1+z)$ is the source frequency, dE_{GW}/df is the energy spectrum emitted by a single binary, $R_m(z, \theta_k)$ is the binary merger rate per unit comoving volume per unit time, where we have assumed the value $R_m(z, \theta_k) = 1540 \text{ Gpc}^{-3} \text{ yr}^{-1}$. We use $\Omega_M = 1 - \Omega_\Lambda = 0.308$ in this paper.

The relation between dE_{GW}/df and gravitational wave amplitude is

$$\frac{dE_{\text{GW}}}{df} = \frac{4\pi^2}{5} f^2 h_{+,m}^2(f) d^2 = \frac{4\pi^2}{5} f^2 h_{\times,m}^2(f) d^2, \quad (\text{A13})$$

where $h_{+,m}(f)$ is defined as the Fourier transform of $h_{+,m}(t)$ and $h_{+,m}$ is the gravitational wave amplitudes along their maximally-emitting directions.

In principle θ_k here covers source parameters such as the component masses, spins, etc., and the total Ω_{GW} has to average over the distribution of these source parameters. Because of limited number of numerical simulations for different EOS and component masses available, we have to make assumptions to facilitate the calculation. In the main text of this article, we have assumed that all binaries comprise a pair of $1.35M_\odot$ neutron stars. Here we investigate a different scenario, where we assume that the component masses of the binary follow the distribution in Eq. (A9). In addition, we assume that the amplitude of different modes in the post-merger stage for a generic binary $m_1 + m_2$ is the same as the ‘‘canonical’’ $1.35 + 1.35M_\odot$ neutron star binary, except that their fre-

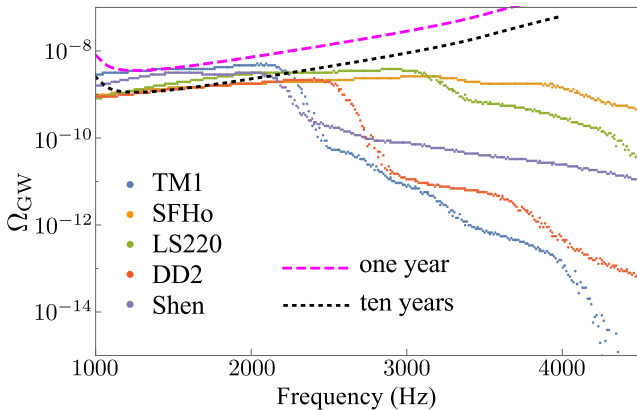


FIG. 15. Gravitational wave background due to post-merger oscillations of binary neutron stars, with component masses sampled according to Eq. (A9) and waveform spectrum scaled as in Eq. (A14). The scattered points are due to finite Monte-Carlo samples generated using Eq. (A9).

quencies are shifted according to

$$f'_{\text{mode},i} = f_{\text{mode},i} \frac{m_1 + m_2}{2.7M_\odot}. \quad (\text{A14})$$

Notice that this assumption on mode frequency is a good approximation for the 22 mode, as shown in Eq. (A10). We plot the new stochastic gravitational wave background generated using Eq. (A9) and Eq. (A14) in Fig. 15, assuming one-year or ten-year observation period with two co-located, co-orientated high frequency detectors. Comparing to Fig. 3 in the main text, Fig. 15 is slightly smoother in its variations, which is due to the average over shifted spectrum for different component masses. The overall amplitude and qualitative behaviour are very similar for these two plots.

6. Neutron star-black hole binary

The merger and ringdown waveform of neutron star/black hole mergers can be classified into three categories [49], based on the relative mass of the two compact objects and the compactness of the star. In the first case, the star is disrupted outside the ISCO (Innermost Stable Circular Orbit), and the subsequent mass inflow produces weak gravitational waves that the waveform ‘‘shuts off’’ quickly from merger. The waveform is well fitted by

$$h(f) = h_{3PN}(f) e^{-(f/f_{\text{cut}})^\sigma}, \quad (\text{A15})$$

where f_{cut} and σ are given by fitting to the numerical waveforms. In the second case, the star is disrupted within the ISCO, and the post-merger waveform still differs significantly from ringdown waveforms of binary BH merger. In the last case, the star is swallowed by the BH, and the post merger waveform is close to the ringdown waveform of binary BH merger. These type II and type III waveforms can be parametrized by

$$h(f) = h_{3PN}(f) e^{-(f/f_{\text{ins}})^\sigma} + \frac{AM}{df} e^{-(f/f_{\text{cut}})^\sigma} (1 - e^{-(f/f_{\text{ins}2})^5}), \quad (\text{A16})$$

where the parameters $f_{\text{ins}}, f_{\text{ins}2}, f_{\text{cut}}, A, \sigma_{\text{cut}}$ are obtained from fitting with numerical waveforms, and d is distance to earth. Following the discussions in [49], we assume that the post-merger process starts at f_{cut} , which is the frequency at which tidal disruption begins for type I, II waveforms. For type III waveforms tidal disruption never happens, and f_{cut} is close to the quasinormal frequency of the final black hole.

TABLE IV. Parameters for different types of BH-NS mergers

Type	$M_{\text{BH}}/M_{\text{NS}}$	$f_{\text{ins}}M$	$f_{\text{ins}2}M$	A	$f_{\text{cut}}M$	σ_{cut}
I	1.5				0.03	2.2
I	2				0.038	2.2
II	3	0.014	0.014	0.13	0.063	2.9
III	4	0.016	0.016	0.103	0.079	4.6
III	5	0.019	0.02	0.09	0.087	3.7

In Table. IV we list the value of BH-NS waveform parameters obtained from [49] and used for generating Table. II in the main text. Here M is the total mass of the binary: $M = M_{\text{BH}} + M_{\text{NS}}$, with the neutron star mass fixed to be $1.35M_{\odot}$ and compactness fixed to be $M_{\text{NS}}/R_{\text{NS}} = 0.145$ assuming $\Gamma = 2$ polytropic EOS.

7. Measuring H_0 without electromagnetic counterparts

Binary neutron star mergers can be used to measure the Hubble Constant without the information of electromagnetic counterparts, either due to a catalog of events for statistically identifying host galaxies [14] or performing mass distribution reconstruction [15], or through a precise tidal effect measurement in the inspiral stage [16], assuming EOS is known. In this work, we follow the discussion in [13] about another possibility, that the redshift information can be obtained by comparing inspiral and post-merger waveforms.

Since only close BNS systems will have their post-merger waveform detected, we can use $z = H_0 d$ to estimate the accuracy of measuring H_0 . We have

$$\delta H_0 = H_0 \sqrt{\left(\frac{\delta z}{z}\right)^2 + \left(\frac{\delta d}{d}\right)^2} = \sqrt{(\delta H_0^z)^2 + (\delta H_0^d)^2}. \quad (\text{A17})$$

For the sources considered here, the accuracy in distance measurement should reach percent level precision, which is much smaller than the redshift-related uncertainty δH_0^z . So we approximate $\delta H_0 \approx \delta H_0^z$.

The post-merger waveforms for BNS with same mass ratio but different total mass are different, and the redshift-scaling on masses in the inspiral stage no longer holds here. This is the key to break the degeneracy in redshift. Because the theoretical uncertainty in modelling the entire post-merger waveform at present, we only discuss how to use 22 peak mode to measure the redshift. In the future when theoretical uncertainties are significantly reduced, the entire post-merger waveform can be used for this purpose to obtain more precise measurement.

For 22 mode, if the EOS is known, its frequency can be inverted to obtain the total mass using Eq. (A10) ($f_{\text{peak,m}}$ is the measured redshifted frequency on earth):

$$\frac{M}{M_{\odot}} = \frac{(1+z)f_{\text{peak,m}}}{1\text{kHz}} \left[a_2 \left(\frac{R_{1.6M_{\odot}}}{1\text{km}} \right)^2 + a_1 \frac{R_{1.6M_{\odot}}}{1\text{km}} + a_0 \right]^{-1}. \quad (\text{A18})$$

On the other hand, the redshifted chirp mass \mathcal{M}_z can be measured with high precision from the inspiral waveform

$$\mathcal{M}_z = (1+z)M\eta^{5/3}, \quad (\text{A19})$$

where $\eta = m_1 m_2 / M^2$ is the symmetric mass ratio, which can also be determined to at least percent level accuracies (so we approximate them as known number here). By comparing the

above two equations, we see that

$$\frac{\delta f_{\text{peak,m}}}{f_{\text{peak,m}}} \approx \frac{\delta(1+z)^2}{(1+z)^2} \approx 2\delta z. \quad (\text{A20})$$

In other words,

$$\begin{aligned} \frac{\delta z}{z} &= \frac{\delta H_0^z}{H_0} \approx \frac{\delta f_{\text{peak,m}}}{f_{\text{peak,m}}} \frac{1}{2H_0 d} \\ &\approx \frac{1}{Q \text{SNR}_{22}} \frac{1}{2H_0 d}. \end{aligned} \quad (\text{A21})$$

where the last line comes from the discussion in [8], Q is the quality factor of the 22 peak (depending on the EOS). Since SNR_{22} is proportional to $1/d$, we find that $\delta z/z$ is independent of the source distance.

We can evaluate Eq. (A21) for different EOS, for which we obtain

$$\frac{\delta H_0^z}{H_0} \equiv N^{-1/2} \times \begin{cases} 8\%, & \text{TM1,} \\ 17\%, & \text{SFHo,} \\ 6\%, & \text{LS220,} \\ 53\%, & \text{DD2,} \\ 12\%, & \text{Shen,} \end{cases} \quad (\text{A22})$$

where N is number of events collected for this purpose. The performance of this approach crucially depends on the quality factor of the 22 peak and the mode amplitude. For most EOS listed here, the measurement accuracy on H_0 after one year observation time may be comparable to or even better than other methods [67]. To include low-SNR events, the above (Fisher type) estimation has to be replaced by a proper Bayesian analysis in which the posterior distribution of H_0 can be constructed based on multiple events.

8. Other astrophysical sources

Another set of high-frequency gravitational wave sources comprise rotating/oscillating neutron stars in our own galaxy. For example, rapidly rotating pulsars may generate gravitational wave at twice of its rotation frequency to be above 1 kHz. Moreover, isolated neutron stars have a zoo of modes in the high frequency range [68], that are astrophysically relevant. For example, f modes of neutron stars could be excited during a violent process, e.g., a giant flare event from a magnetar. Following the analysis in [57], the SNR of such f-mode oscillation using the high-frequency gravitational wave detector can be estimated as

$$\begin{aligned} \text{SNR} &\approx 1.2 \alpha \left(\frac{2000\text{Hz}}{f_{\text{mode}}} \right)^2 \left(\frac{S_h}{2.8 \times 10^{-49}\text{Hz}^{-1}} \right)^{-1/2} \left(\frac{B}{10^{15}\text{G}} \right)^2 \\ &\left(\frac{1\text{kpc}}{d} \right) \left(\frac{R}{10\text{km}} \right)^2 \left(\frac{0.07M_{\odot}}{m_n} \right)^{1/2}, \end{aligned} \quad (\text{A23})$$

where f_{mode} is the frequency of the f mode, m_n is the effective mass of the mode (see [57]), R is the star radius, B is the strength of external magnetic field, and $\alpha \sim 1$ is the overlapping function between the mode of external driving.

Given the fact the closest magnetar flare observed so far comes from a distance at ~ 6.1 kpc (SGR 1900 + 14), it is then conceivable to detect such an oscillation, if a closer active magnetar can be discovered in the future, and that the sensitivity of the detector can be further improved by a factor of ~ 5 . Such improvement may be achieved by implementing longer arm lengths. Note that there are three magnetar observed in the past 40 years from the most active three Galactic magnetars, so the time separation between giant flares for a given active magnetar can be estimated as ~ 40 years.

This type of source is particularly interesting because a gravitational-wave observation of the star's oscillation may be associated with the energetic X-ray emissions during the giant flare phase and/or subsequent quasi periodic oscillations [69].

For core-collapse supernovae, the dominant spectra power reside at frequency below 1 kHz. However, the high or-

der modes also contains crucial information about the post-bounce dynamical processes [70]. Following Fig. 8 of [70], we approximate the amplitude of high-frequency (> 1 kHz) GW as

$$h \sim 10^{-20} \beta \left(\frac{10 \text{ kpc}}{d} \right) \left(\frac{f}{10^3 \text{ kHz}} \right)^{-\alpha}, \quad (\text{A24})$$

where α is roughly between 3 and 4. The corresponding SNR for the entire high-frequency part of the waveform is

$$\text{SNR}^2 = 4 \int_{1 \text{ kHz}}^{\infty} \frac{h^2}{S_{hf}} \frac{df}{f}, \quad (\text{A25})$$

which leads to

$$\text{SNR} \approx 6\beta \times \frac{4}{\alpha + 1} \left(\frac{1 \text{ Mpc}}{d} \right) \left(\frac{S_h}{2.8 \times 10^{-49} \text{ Hz}^{-1}} \right)^{-1/2}. \quad (\text{A26})$$

-
- [1] The LIGO Scientific Collaboration and The Virgo Collaboration, *Phys. Rev. Lett.* **119**, 161101 (2017).
- [2] L. Li and B. Paczyński, *Astrophys. J. Lett.* **507**, L59 (1998).
- [3] S. Rosswog, *Astrophys. J.* **634**, 1202 (2005).
- [4] B. Metzger, G. Martínez-Pinedo, S. Darbha, E. Quataert, A. Arcones, D. Kasen, R. Thomas, P. Nugent, I. Panov, and N. Zinner, *MNRAS* **406**, 2650 (2010).
- [5] The LIGO Scientific Collaboration and The Virgo Collaboration, *Astrophys. J. Lett.* **848**, L12 (2017).
- [6] The LIGO Scientific Collaboration and The Virgo Collaboration, *Astrophys. J. Lett.* **848**, L13 (2017).
- [7] The LIGO Scientific Collaboration and The Virgo Collaboration, *The Astrophysical Journal* **850**, L39 (2017).
- [8] H. Yang, V. Paschalidis, K. Yagi, L. Lehner, F. Pretorius, and N. Yunes, [arXiv:1707.00207](https://arxiv.org/abs/1707.00207) (2017).
- [9] J. Clark, A. Bauswein, L. Cadonati, H. T. Janka, C. Pankow, and N. Stergioulas, *Phys. Rev. D* **90**, 62004 (2014).
- [10] V. Paschalidis, W. E. East, F. Pretorius, and S. L. Shapiro, *Phys. Rev. D* **92**, 121502 (2015).
- [11] W. E. East, V. Paschalidis, F. Pretorius, and S. L. Shapiro, *Phys. Rev. D* **93**, 24011 (2016).
- [12] L. Lehner, S. L. Liebling, C. Palenzuela, and P. M. Motl, *Phys. Rev. D* **94**, 43003 (2016).
- [13] C. Messenger, K. Takami, S. Gossan, L. Rezzolla, and B. S. Sathyaprakash, *Phys. Rev.* **X4**, 041004 (2014), [arXiv:1312.1862 \[gr-qc\]](https://arxiv.org/abs/1312.1862).
- [14] B. F. Schutz, *nature* **323**, 310 (1986).
- [15] S. R. Taylor, J. R. Gair, and I. Mandel, *Phys. Rev. D* **85**, 23535 (2012).
- [16] C. Messenger and J. Read, *Phys. Rev. Lett.* **108**, 91101 (2012).
- [17] R. X. Adhikari, *Rev. Mod. Phys.* **86**, 121 (2013).
- [18] The LIGO Scientific Collaboration, *Nature Physics* **7**, 962 (2011).
- [19] The LIGO Scientific Collaboration, *Nature Photonics* **7**, 613 (2013).
- [20] R. Schnabel, *Physics Reports* **684**, 1 (2017).
- [21] B. J. Meers, *Phys. Rev. D* **38**, 2317 (1988).
- [22] A. Buonanno and Y. Chen, *Phys. Rev. D* **64**, 042006 (2001).
- [23] S. Hild, H. Grote, M. Hewitson, H. Lück, J. R. Smith, K. A. Strain, B. Willke, and K. Danzmann, *Class. Quant. Grav.* **24**, 1513 (2007).
- [24] A. Thüring, R. Schnabel, H. Lück, and K. Danzmann, *Optics letters* **32**, 985 (2007).
- [25] H. Miao, Y. Ma, C. Zhao, and Y. Chen, *Phys. Rev. Lett.* **115**, 211104 (2015).
- [26] M. Page, J. Qin, J. La Fontaine, C. Zhao, and D. Blair, [arXiv:1711.04469](https://arxiv.org/abs/1711.04469) (2017).
- [27] H. J. Kimble, Y. Levin, A. B. Matsko, K. S. Thorne, S. P. Vyatchanin, H. J. Kimble, Y. Levin, A. B. Matsko, K. S. Thorne, and S. P. Vyatchanin, *Phys. Rev. D* **65**, 022002 (2001).
- [28] E. Oelker, T. Isogai, J. Miller, M. Tse, L. Barsotti, N. Mavalvala, and M. Evans, *Phys. Rev. Lett.* **116**, 041102 (2016).
- [29] R. X. Adhikari, N. Smith, A. Brooks, L. Barsotti, B. Shapiro, B. Lantz, D. McClelland, E. K. Gustafson, D. V. Martynov, V. Mitrofanov, D. Coyne, K. Arai, C. Torrie, and C. Wipf, *LIGO DCC-T1400226* (2017).
- [30] M. Punturo, M. Abernathy, F. Acernese, B. Allen, N. Andersson, K. Arun, F. Barone, B. Barr, and Others, *Classical and Quantum Gravity* **27**, 194002 (2010).
- [31] The LIGO Scientific Collaboration, *Classical and Quantum Gravity* **34**, 44001 (2017).
- [32] The LIGO Scientific Collaboration, *Classical and Quantum Gravity* **32**, 74001 (2015).
- [33] F. Acernese, M. Agathos, K. Agatsuma, D. Aisa, N. Allemandou, A. Allocca, J. Amarni, P. Astone, G. Balestri, G. Ballardini, F. Barone, J.-P. Baronick, M. Barsuglia, A. Basti, F. Basti, T. S. Bauer, V. Bavigadda, M. Bejger, M. G. Beker, C. Belczynski, D. Bersanetti, A. Bertolini, M. Bitossi, M. A. Bizouard, S. Bloemen, M. Blom, M. Boer, G. Bogaert, D. Bondi, F. Bondu, L. Bonelli, R. Bonnand, V. Boschi, L. Bosi, T. Bouedo, C. Bradaschia, M. Branchesi, T. Briant, A. Brillet, V. Brisson, T. Bulik, H. J. Bulten, D. Buskulic, C. Buy, G. Cagnoli, E. Calloni, C. Campeggi, B. Canuel, F. Carbognani, F. Cavalier, R. Cavalieri, G. Cella, E. Cesarini, E. C. Mottin, A. Chincarini, A. Chiummo, S. Chua, F. Cleva, E. Coccia, P.-F. Cohadon, A. Colla, M. Colombini, A. Conte, J.-P. Coulon,

- E. Cuoco, A. Dalmaz, S. D'Antonio, V. Dattilo, M. Davier, R. Day, G. Debreczeni, J. Degallaix, S. Deléglise, W. D. Pozzo, H. Dereli, R. D. Rosa, L. D. Fiore, A. D. Lieto, A. D. Virgilio, M. Doets, V. Dolique, M. Drago, M. Ducrot, G. Endr aczi, V. Fafone, S. Farinon, I. Ferrante, F. Ferrini, F. Fidecaro, I. Fiori, R. Flamini, J.-D. Fournier, S. Franco, S. Frasca, F. Frasconi, L. Gammaitoni, F. Garufi, M. Gaspard, A. Gatto, G. Gemme, B. Gendre, E. Genin, A. Gennai, S. Ghosh, L. Giacobone, A. Giazotto, R. Gouaty, M. Granata, G. Greco, P. Groot, G. M. Guidi, J. Harms, A. Heidmann, H. Heidmann, P. Hello, G. Hemming, E. Hennes, D. Hofman, P. Jaranowski, R. J. G. Jonker, M. Kasprzack, F. K ef elien, I. Kowalska, M. Kraan, A. Kr olak, A. Kutynia, C. Lazzaro, M. Leonardi, N. Leroy, N. Letendre, T. G. F. Li, B. Lieunard, M. Lorenzini, V. Lorette, G. Losurdo, C. Magazz , E. Majorana, I. Maksimovic, V. Malvezzi, N. Man, V. Mangano, M. Mantovani, F. Marchesoni, F. Marion, J. Marque, F. Martelli, L. Martellini, A. Masserot, D. Meacher, J. Meidam, F. Mezzani, C. Michel, L. Milano, Y. Minenkov, A. Moggi, M. Mohan, M. Montani, N. Morgado, B. Mours, F. Mul, M. F. Nagy, I. Nardecchia, L. Naticchioni, G. Nelemans, I. Neri, M. Neri, F. Nocera, E. Pacaud, C. Palomba, F. Paoletti, A. Paoli, A. Pasqualetti, R. Passaquieti, D. Passuello, M. Perciballi, S. Petit, M. Pichot, F. Piergiovanni, G. Pillant, A. Piluso, L. Pinard, R. Poggiani, M. Prijatelj, G. A. Prodi, M. Punturo, P. Puppo, D. S. Rabeling, I. R acz, P. Rapagnani, M. Razzano, V. Re, T. Regimbau, F. Ricci, F. Robinet, A. Rocchi, L. Rolland, R. Romano, D. Rosi nska, P. Ruggi, E. Saracco, B. Sassolas, F. Schimmel, D. Sentenac, V. Sequino, S. Shah, K. Siellez, N. Straniero, B. Swinkels, M. Tacca, M. Tonelli, F. Travasso, M. Turconi, G. Vajente, N. van Bakel, M. van Beuzekom, J. F. J. van den Brand, C. Van Den Broeck, M. V. van der Sluys, J. van Heijningen, M. Vas uth, G. Vedovato, J. Veitch, D. Verkindt, F. Vetrano, A. Vicer , J.-Y. Vinet, G. Visser, H. Vocca, R. Ward, M. Was, L.-W. Wei, M. Yvert, A. Z.  zny, and J.-P. Zendri, *Classical and Quantum Gravity* **32**, 024001 (2015).
- [34] Y. Aso, Y. Michimura, K. Somiya, M. Ando, O. Miyakawa, T. Sekiguchi, D. Tatsumi, and H. Yamamoto, *Phys. Rev. D* **88**, 43007 (2013).
- [35] H. Yu, D. Martynov, S. Vitale, and M. Evans, *LIGO DCC-P1700394* (2017).
- [36] H. Miao and M. Evans, *LIGO DCC-P1700202* (2017).
- [37] S. M. Aston, M. A. Barton, A. S. Bell, N. Beveridge, B. Bland, A. J. Brummitt, G. Cagnoli, C. A. Cantley, L. Carbone, A. V. Cumming, L. Cunningham, R. M. Cutler, R. J. S. Greenhalgh, G. D. Hammond, K. Haughian, T. M. Hayler, A. Heptonstall, J. Heefner, D. Hoyland, J. Hough, R. Jones, J. S. Kissel, R. Kumar, N. A. Lockerbie, D. Lodhia, I. W. Martin, P. G. Murray, J. O'Dell, M. V. Plissi, S. Reid, J. Romie, N. A. Robertson, S. Rowan, B. Shapiro, C. C. Speake, K. A. Strain, K. V. Tokmakov, C. Torrie, A. A. van Veggel, A. Vecchio, and I. Wilmot, *Classical and Quantum Gravity* **29**, 235004 (2012).
- [38] T. Corbitt, C. Wipf, T. Bodiya, D. Ottaway, D. Sigg, N. Smith, S. Whitcomb, and N. Mavalvala, *Phys. Rev. Lett.* **99**, 160801 (2007).
- [39] W. Z. Korth, H. Miao, T. Corbitt, G. D. Cole, Y. Chen, and R. X. Adhikari, *Phys. Rev. A* **88**, 033805 (2013).
- [40] H. Vahlbruch, M. Mehmet, K. Danzmann, and R. Schnabel, *Phys. Rev. Lett.* **117**, 110801 (2016).
- [41] Z. Liu, P. Fulda, M. A. Arain, L. Williams, G. Mueller, D. B. Tanner, and D. H. Reitze, *Appl. Opt.* **52**, 6452 (2013).
- [42] G. D. Cole, W. Zhang, M. J. Martin, J. Ye, and M. Aspelmeyer, *Nature Photonics*, 644 (2013).
- [43] G. M. Harry, T. P. Bodiya, and R. DeSalvo, *Optical coatings and thermal noise in precision measurement* (Cambridge University Press, 2012).
- [44] J. Harms, Y. Chen, S. Chelkowski, A. Franzen, H. Vahlbruch, K. Danzmann, and R. Schnabel, *Phys. Rev. D* **68**, 42001 (2003).
- [45] Y. Ma, H. Miao, B. Pang, M. Evans, C. Zhao, J. Harms, R. Schnabel, and Y. Chen, *Nature Physics* **13**, 776 (2017).
- [46] S. Bose, K. Chakravarti, L. Rezzolla, B. S. Sathyaprakash, and K. Takami, *arXiv:1705.10850* (2017).
- [47] F.  zel and P. Freire, *Annual Review of Astronomy and Astrophysics* **54**, 401 (2016).
- [48] H. Yang, W. E. East, and L. Lehner, *arXiv:1710.05891* (2017).
- [49] M. Shibata, K. Kyutoku, T. Yamamoto, and K. Taniguchi, *Phys. Rev. D* **79**, 44030 (2009).
- [50] E. Thrane and J. D. Romano, *Phys. Rev. D* **88**, 124032 (2013).
- [51] X.-J. Zhu, E. J. Howell, D. G. Blair, and Z.-H. Zhu, *Mon. Not. Roy. Astron. Soc.* **431**, 882 (2013), *arXiv:1209.0595 [gr-qc]*.
- [52] Q. Cheng, S.-N. Zhang, and X.-P. Zheng, *Phys. Rev. D* **95**, 83003 (2017).
- [53] S. Marassi, R. Ciolfi, R. Schneider, L. Stella, and V. Ferrari, *MNRAS* **411**, 2549 (2011).
- [54] A. Wicht, K. Danzmann, M. Fleischhauer, M. Scully, G. M uller, and R. Rinkelff, *Optics Communications* **134**, 431 (1997).
- [55] Y. Ma, H. Miao, C. Zhao, and Y. Chen, *Phys. Rev. A* **92**, 023807 (2015).
- [56] M. Zhou, Z. Zhou, and S. M. Shahriar, *Phys. Rev. D* **92**, 082002 (2015).
- [57] Y. Levin and M. van Hoven, *MNRAS* **418**, 659 (2011).
- [58] S. L. Danilshin and F. Y. Khalili, *Living Reviews in Relativity* **15** (2012).
- [59] H. Miao, H. Yang, R. X. Adhikari, and Y. Chen, *Class. Quant. Grav.* **31**, 165010 (2014).
- [60] Y. Chen, *Journal of Physics B: Atomic, Molecular and Optical Physics* **46**, 104001 (2013).
- [61] C. Palenzuela, S. L. Liebling, D. Neilsen, L. Lehner, O. L. Caballero, E. O'Connor, and M. Anderson, *Phys. Rev. D* **92**, 44045 (2015).
- [62] K. Kiuchi, Y. Sekiguchi, M. Shibata, and K. Taniguchi, *Phys. Rev. Lett.* **104**, 141101 (2010).
- [63] N. Stergioulas, A. Bauswein, K. Zagkouris, and H.-T. Janka, *Mon. Not. Roy. Astron. Soc.* **418**, 427 (2011).
- [64] A. Bauswein, N. Stergioulas, and H.-T. Janka, *Eur. Phys. J.* **A52**, 56 (2016).
- [65] B. S. Sathyaprakash and B. F. Schutz, *Living Reviews in Relativity* **12** (2009).
- [66] A. Bauswein, N. Stergioulas, and H. T. Janka, *Phys. Rev. D* **90**, 23002 (2014).
- [67] W. Del Pozzo, T. G. F. Li, and C. Messenger, *Phys. Rev. D* **95**, 43502 (2017).
- [68] N. Andersson and K. D. Kokkotas, *MNRAS* **299**, 1059 (1998).
- [69] C. Thompson, H. Yang, and N. Ortiz, *Astrophys. J.* **841**, 54 (2017).
- [70] C. D. Ott, *Class. Quantum Grav.* **26**, 63001 (2009).